Thermal Convection in a Tilted Cell

Panyu Chen[1]

[1]NYU-ECNU Institute of Mathematical Sciences at NYU Shanghai

May 2023

Abstract

In the Rayleigh-Bénard convection model of incompressible buoyancy-driven fluids in a square cell, fluid motion is highly dependent on the temperature field. Temperature differences across the cell can cause variations in fluid densities and eventually lead to turbulence around the cell. Here, we approach the problem of intervening fluid circulation and controlling heat transport by tilting the whole cell. We mathematically express our tilted convection model with Navier-Stokes equations within Boussinesq approximation. We solve the equations by numerical methods and derive the Reynolds number Re, Nusselt number Nu, and the net angular momentum which reflect fluid motions and heat transfer within the system. It's discovered that circular activities gradually diminish as α grows, and heat transport efficiency is maximized when heat and cooling sources are applied on vertical walls before dropping at higher α degrees. Our findings provide inspirations for real life scenarios of controlling fluid activities and heat transfer.

Contents

1 Introduction

Fluid activities and heat transfer in thermal convection systems have always been widely concerned and studied as they're applicable to a broad range of scientific and industrial problems in our real life [2]. For example, both the enhancing [28] and suppressing [9], [15] of heat transportation are crucial topics included in comprehensive chemistry, biology, and engineering aspects, such as designing efficient heating device or achieving effective ventilation in buildings and rooms. It's also encountered in natural processes [30] like crustal movements, ocean currents, and monsoons. The general pursuit of understanding and controlling thermal convection in fluid turbulence has cultivated extensive scientific research which studies thermal convection and diffusion in fluids, and yet the question remains how to analyze the complicated dynamics of heat-carrying fluid flows within a model that well simplifies natural reality.

The Rayleigh-Bénard convection model is a typical and common-studied model that describes an ideal fluid container fixed to a heating and cooling source [18]. As the density lowers along with the heating of fluids, the buoyant force promotes the hotter fluids to elevate while colder fluids submerge, causing turbulence and even large scale circulation to form in specific viscosity and thermal diffusivity settings. A variety of subsequent research is based on the model in studying turbulence that carries heat across fluids and proposing relevant methods to control the overall heat transfer in the system. Among all these studies, a great diversity of methods have been proposed to change thermal convection by toggling the physical properties of the convection system.

For instance, there have been research that focuses on introducing oscillatory flow pulsation to the cell [21], [29]. Alternatively, a series of studies have concentrated on the influence of surface roughness upon thermal convection, aiming to enhance heat transport [10], to examine whether heat flux decreases may happen in specific cases [11], [31], or to facilitate the "ultimate regime" where heat transport is independent from fluid molecular properties [24], [38]. Such approaches to roughness have been similarly applied to assess shear effects in a cell [7], [16]; or the effects of means of confinement inserted in the cell like partition walls [4], [9], narrowed cell width [14], or direct adjustments of the size (aspect ratio) of the cell [26].

Studies have also focused on controlling thermal boundary conditions [13] of the convection system. Specific approaches include adding extra heat sources to the sidewalls of the cell [34], imposing a horizontal flux [19], and even configuring oscillatory sidewall temperatures [32], [35], [36]. In this way, researchers can examine how the top/bottom heating/cooling sources in the classical Rayleigh-Bénard model can interact with the newly introduced temperature configurations.

Researchers have also considered the physical properties of fluids and put them into use. Apart from

nanofluids [8], polymer [5], and particles [3], [33], studies have also concerned turbulence in multiphase fluids [6], [28], [17], [33], which essentially add new factors that decide the fluid density (and the forcing upon it) apart from the scalar temperature value [9]. Besides changing inherent physical properties of the container and the fluids, scientists have also made attempts imparting dynamic operations to the cell. The cell can be rotated [22], [37], [9] about the vertical axis at certain ranges (the inverse Rossby-number range) of angular speeds, or vertically vibrated [30] so that the vibrations interfere with the motions of buoyancy-driven fluids. In the end, all adjustments and operations formulated and implemented are extendable to real life strategies in industry and engineering to control dynamic fluid activities and enhance heat transfer. From a broader view, a great level of freedom has been left to nowadays researchers to find their own ways adjusting the model. In our study, we've chosen the approach of tilting the entire cell and examining how the thermal convection is influenced by different tilting angles.

We refer to studies conducting similar tilting operations in recording both the vertical heat flux (Nusselt Number Nu) [27] passing through the cell and the Reynolds number Re implying the activeness of turbulent fluids in the cell [12], given different tilting angles. In this way, we draw a complete picture of flowing incompressible fluids carrying heat in a tilted square cell. Nonetheless, instead of composing the Oberbeck-Boussinesq equations to model the convection system [27], we refer to [19] and construct our own Navier-Stokes equations to describe the system.

In the following sections, we'll present how we analyze the impacts of convection-cell-tilting on fluid motions and how it's intercorrelated with enhanced or reduced heat transfer within the cell. In section 2 we derive the concepts of vorticity and streamfucntion from velocity, and we compose the Navier-Stokes-Boussinesq equations along with the heat equation to describe the dynamics of fluid velocity and temperature. Then, in section 3 we discretize the equations and convert them into Helmholtz equations solvable by matrix methods. Finally, in section 4 we extract the Reynolds number Re, Nusselt number Nu, and the system total angular momentum from the equation solutions so that we can interpret the distinct modes of motion and heat transfer of the fluids at different tilting angles.

2 Model Formulation

We refer to [1] in establishing a model for fluid dynamics inside the cell. A preliminary set of Navier-Stokes equations is written to elucidate the relation between fluid velocity, pressure, and the buoyant force. We apply Boussinesq approximation to the equations to introduce the influence of temperature and density

in the dynamical system, and we also compose the energy equation to describe how temperatures at different locations in the system change along time. To make the system of equations solvable, we introduce the crucial concepts of vorticity and stream-function in representing velocity. In section 3, the partial differential equations for temperature, vorticity, and stream-function will be discretized and solved by numerical methods to indicate the flowing of fluids and energy flux at every time step in each part of the convection cell.

2.1 Euler's Equations

The Navier-Stokes equation derives from the Euler's equation of motions [1] which focuses on a unit blob flowing inside the cell, whose location $\mathbf{x}$ can be considered as a function of time t. The Euler's equation describes that the rate of change of flow velocity of the blob is decided by the buoyant force and the pressuring of surrounding fluids. We start with proving the equation inside the classical Rayleigh-Bénard convection model which is untilted ($\alpha = 0^\circ$), and later we'll modify the model for the case of a non-zero tilting angle.

Theorem 1 (Euler's Equations)**.** *For a unit blob at time t and location $\boldsymbol{x} = (x(t), y(t))$ in an untilted Rayleigh-Bénard convection cell, the total differential of its flow velocity $\mathbf{u}(x, y, t) = \begin{pmatrix} u(x,y,t) & v(x,y,t) \end{pmatrix}^T$ depends on fluid density ρ, pressure ∇p exerted by surrounding fluids, and the buoyant force represented by the gravitational term $\boldsymbol{g} = \begin{pmatrix} 0 & g \end{pmatrix}^T$ where g is the gravitational acceleration.*

$$\frac{D\boldsymbol{u}}{Dt} = -\frac{\nabla p}{\rho} + \boldsymbol{g}, \tag{1}$$

$$\nabla \cdot \boldsymbol{u} = 0. \tag{2}$$

Proof. Taking an arbitrary domain of fluids inside the cell with mass m, volume V and surface boundary $S = \partial V$, by second Newton's Law, we can write the equation for the total differential of $\mathbf{u}$ as

$$m\frac{D\mathbf{u}}{Dt} = F_{\text{pressuring}} + F_{\text{buoyancy}}, \tag{3}$$

where $m = \rho V$, $F_{\text{pressuring}}$ describes the pressure force from surrounding fluids and F_{buoyancy} describes the buoyant force.

According to Archimedes' principle,

$$F_{\text{buoyancy}} = \rho V \mathbf{g}. \tag{4}$$

Denoting $\mathbf{n}$ as the unit vector normal to blob surface S, then the pressure force imparted to the fluids is

$$F_{\text{pressuring}} = -\oint_S p \cdot \mathbf{n}\, dS = -\int_V \nabla p\, dV. \tag{5}$$

Reducing the domain to a sufficiently small blob of fluid so that ∇p is assumed to be invariant, the pressure force is then simplified to $-\nabla pV$. Now, applying 4 and 5 to 3, we finally compose the equation

$$\rho V \frac{D\mathbf{u}}{Dt} = (-\nabla p + \rho \mathbf{g})V. \tag{6}$$

which derives the equation 1.

As for the proof of 2, check that the volume of incompressible fluid leaving the domain is written as $\oint_S \mathbf{u}\cdot\mathbf{n}\, dS$ which should be zero on account of incompressibility, giving the equation

$$\oint_S \mathbf{u} \cdot \mathbf{n}\, dS = \int_V \nabla \cdot \mathbf{u}\, dV = 0. \tag{7}$$

which, reducing the domain to a unit blob, derives the incompressibility condition 2. This completes our proof of 1 and 2. □

2.2 Navier-Stokes Equations

The formulation of the Euler's equation 1 in the classical Rayleigh-Bénard model leads to the Navier-Stokes Equation in a tilted convection model by modifying the gravitational term $\mathbf{g}$, expanding $\frac{D\mathbf{u}}{Dt}$, and introducing the viscosity term ν. The analysis of a dyed blob wandering inside the cell provides us information of fluid velocities at every location of the whole cell, and the information dynamically changes through time.

Theorem 2 (Navier-Stokes Equations)**.** *For fluids in a Rayleigh-Bénard convection cell tilted counter-clockwise with angle α at time t and location $\boldsymbol{x} = (x, y)$, we can associate the gradient and time derivative of the fluid velocity $\boldsymbol{u}$ with a series of forcing terms. Eventually the equations are written as*

$$\begin{cases} \boldsymbol{u}_t + (\boldsymbol{u}\cdot\nabla)\boldsymbol{u} + \frac{\nabla p}{\rho} - \nu\Delta\boldsymbol{u} = \begin{pmatrix} g\sin(\alpha) & g\cos(\alpha) \end{pmatrix}^T, \\ \nabla \cdot \boldsymbol{u} = 0. \end{cases} \tag{8}$$

Proof. As mentioned above, the rate of change of flow velocity $\frac{D\mathbf{u}(x(t),y(t),t)}{Dt}$ describes the changing velocity

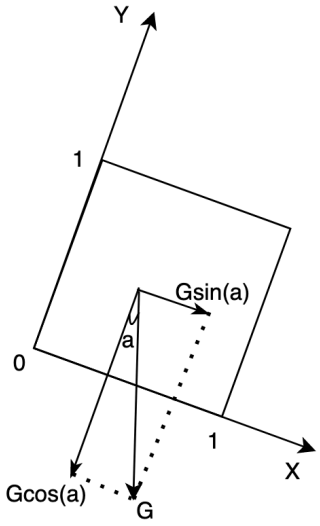

Figure 1: Gravitational Impact upon Tilted Convection Cell

of a flowing dyed blob whose location $\mathbf{x} = \begin{pmatrix} x(t) & y(t) \end{pmatrix}$ is regarded as a function of time. Writing $\mathbf{u} = \begin{pmatrix} u & v \end{pmatrix}^T$, we can therefore expand the rate of change of flow velocity:

$$\frac{D\mathbf{u}}{Dt} = \mathbf{u}_t + u\mathbf{u}_x + v\mathbf{u}_y = \mathbf{u}_t + \mathbf{u} \cdot \nabla \mathbf{u}, \tag{9}$$

where we denote $\mathbf{u}_t = \partial_t \mathbf{u} = \frac{\partial \mathbf{u}}{\partial t}$ (and the similar notations work for other partial derivatives in this paper). Notice that $\mathbf{u}_t$ denotes the rate of change of $\mathbf{u}$ at fixed locations, and $\mathbf{u}_x$ and $\mathbf{u}_y$ describe the changing rate at fixed time along different locations.

As we always regard the x and y axes of our system as parallel to the top and bottom and sides of the convection cell as shown in figure 1, the vertical gravitational term $\mathbf{g}$ is decomposed along the two axes as

$$\hat{\mathbf{g}} = \begin{pmatrix} g\sin(\alpha) & g\cos(\alpha) \end{pmatrix}^T. \tag{10}$$

Applying all modifications to 1, and also taking into account the viscous term $\nu\Delta\mathbf{u}$ eventually gives the Navier-Stokes equations 8. □

2.3 Boussinesq Approximation

We further apply a series of simplifications to our model within Boussinesq approximation to emphasize the role of temperature in changing the concentration of fluids, which further affects buoyancy and fluid velocity. To be specific, we apply the first order Taylor expansion to the density term $\rho(p, T)$ with respect to the variable T and the influence of pressure p is ignored. In this way, we no longer consider ρ as a function of time and space. We eventually obtain the Navier-Stokes-Boussinesq equations.

Theorem 3 (Navier-Stokes-Boussinesq Equations)**.** *For fluids in the Rayleigh-Bénard convection cell modeled by the Navier-Stokes equations 8, the flow velocity* $\boldsymbol{u}$ *is associated with fluid temperature* $T(x, y, t)$ *by:*

$$\begin{cases} \boldsymbol{u}_t + (\boldsymbol{u} \cdot \nabla)\boldsymbol{u} = -\frac{\nabla p}{\rho_0} + \nu\Delta\boldsymbol{u} - \hat{\boldsymbol{g}}(1 - \alpha_T(T - T_0)), \\ \nabla \cdot u = 0, \end{cases} \tag{11}$$

where α_T *is the thermal expansion coefficient and* T_0 *is the reference temperature when the corresponding density takes the value* ρ_0*.*

Proof. Detailed explanations of the Boussinesq approximation can be found in [25]. □

Apart from the velocity equations, we also build the partial differential equation for temperature T in a way similar to our tracking of the velocity of a dyed blob flowing in the cell, and neglecting the dissipation of heat.

Theorem 4 (Heat Equation)**.** *For fluids in the Rayleigh-Bénard convection model with thermal diffusivity* κ_T *and scalar temperature* $T(x(x, y, t)$*, the heat equation is written as:*

$$T_t + (\boldsymbol{u} \cdot \nabla)T = \kappa_T \Delta T. \tag{12}$$

Proof. Modeling a dyed blob with temperature $T(x(t), y(t), t)$, because heat dissipation is ignored, the total differential of T is only related with the thermal diffusivity and the Laplacian of T:

$$\frac{DT}{Dt} = \kappa_T \Delta T. \tag{13}$$

Considering that T is dependent on the functions $x(t)$ and $y(t)$, whose rate of change equate to the velocity

$\mathbf{u}$ of the blob decomposed on the x and y axes, we can expand the total differential in a way similar to the 9:

$$\frac{DT}{Dt} = T_t + uT_x + vT_y = T_t + T \cdot \nabla \mathbf{u}, \tag{14}$$

and the simultaneous equations 13 and 14 derive the equation 12 □

We'll later see the importance of the temperature equation in supporting our solving of the vorticity equation which finally deduces the velocity values.

2.4 Vorticity and Streamfunction

To cancel out the unknown pressure term in the Navier-Stokes-Boussinesq equation 11, we introduce the concept of vorticity ω by applying the curl operator to flow velocity and converting 11 into an equation of ω.

Definition 1 (Vorticity)**.** *For flow velocity* $\boldsymbol{u}$*, the vorticity* ω *is defined as a scalar value satisfying the equation:*

$$\omega \boldsymbol{k} = \nabla \times \boldsymbol{u}, \tag{15}$$

where $\boldsymbol{k}$ *represents the unit vector on a third dimension besides the* x *and* y *dimensions of the cell.*

Theorem 5 (Vorticity Equation)**.**

$$\omega_t + \boldsymbol{u} \cdot \nabla \omega - \nu \Delta \omega = \alpha_T [T_x g \cos(a) - T_y g \sin(a)]. \tag{16}$$

Proof. By the definition of the curl operator, given a 3-dimensional vector $\mathbf{a} = \begin{pmatrix} a & b & c \end{pmatrix}^T$ with cartesian coordinates on the x, y, and z axes, there's that

$$\nabla \times a = \begin{pmatrix} \partial_y c - \partial_z b & \partial_z a - \partial_x c & \partial_x b - \partial_y a \end{pmatrix}^T. \tag{17}$$

Then, considering a 2d-vector term a as a 3d-vector with the value on the z axis as zero, the values on the x and y axes of $\nabla \times a$ are both reduced to zero. In other words, curl operator merges the values of the 2d-vector terms and attributes them to a scalar on the extra z dimension.

Applying the curl operator to each term in 11 and checking the resulting scalar value on the z dimension, the velocity term $\mathbf{u}$ gives ω by definition 15 and the pressure term $\frac{-\nabla p}{\rho_0}$ gives scalar zero. For the gradient

term $\Delta\mathbf{u} = \begin{pmatrix} u_{xx}+u_{yy} & v_{xx}+v_{yy} \end{pmatrix}^T$, there's that

$$\partial_x(v_{xx}+v_{yy}) - \partial_y(u_{xx}+u_{yy}) = \partial^2_{xx}(v_x-u_y) + \partial^2_{yy}(v_x-u_y) = \Delta\omega, \tag{18}$$

and for the gravitational term there is that

$$\nabla \times (\alpha_t(T-T_0)-1) \begin{pmatrix} g\sin(a) & g\cos(a) & 0 \end{pmatrix}^T = \alpha_T[T_x g\cos(a) - T_y g\sin(a)]. \tag{19}$$

To sum up, applying the curl operator to the equation 11 secures the relation 16 for ω. □

However, the lack of boundary data of ω makes the vorticity equation 16 unsolvable, so we have to support our convection model with more equations. Thus, the incompressibility condition 2 leads us to introduce the concept of streamfunction ψ.

Definition 2 (Streamfunction)**.** *For flow velocity $\boldsymbol{u}$, the streamfunction ψ is defined by the curl operator equation:*

$$\boldsymbol{u} = \nabla \times (\psi \cdot \boldsymbol{k}). \tag{20}$$

We can check that the streamfunction ψ is mathematically defined to render the flow velocities on the x and y directions – u and v – as its partial derivatives, and that ψ is associated with vorticity ω by a simple Poisson equation. In this sense, the streamfunction takes much more an abstract mathematical meaning than a practical physical meaning.

Theorem 6 (Streamfunction Equation)**.** *By the definition of vorticity ω and streamfunction ψ, it holds that:*

$$\Delta\psi = -\omega. \tag{21}$$

Proof. Since $\psi\mathbf{k} = \begin{pmatrix} 0 & 0 & \psi \end{pmatrix}^T$, there's that

$$\nabla \times (\psi k) = \begin{pmatrix} \partial_y\psi & -\partial_x\psi & 0 \end{pmatrix}^T. \tag{22}$$

Therefore, applying curl operator to 20 gives:

$$\omega = \nabla \times \mathbf{u} = \nabla \times [\nabla \times (\psi k)] = -\partial^2_{yy}\psi - \partial^2_{xx}\psi = -\Delta\psi. \tag{23}$$

This completes our proof of 21. □

We'll see in the later section 3 how the streamfunction provides sufficient boundary data that makes the vorticity equation solvable. Basically, the Neumann and Dirichlet conditions provided by ψ and temperature T are all the information we have to solve the PDEs 12,16, and 21 and acquire approximate results for the variational temperatures and velocities everytime, everywhere in the cell.

2.5 Nondimensionalization

We refer to [20] in nondimensionalizing the temperature, velocity, vorticity, and streamfunction values which we now denote as θ, $\mathbf{U} = \begin{pmatrix} U & V \end{pmatrix}^T$, Ω, and Ψ. This enables us to neglect the difference in units and amplitudes of the physical terms.

We set the dimensionless convection cell to be a domain $D = [0,1] \times [0,1]$. To make T dimensionless, because the convection cell takes temperature T_1 at the heated bottom and temperature T_2 at the cooled top, we denote $\theta = \frac{T-T_2}{T_1-T_2}$. Since the value of T is interconnected with the values of the other three terms by the equations 12, 16, and 21, we only need to ensure the initial and boundary conditions provided by θ and Ψ are made dimensionless, and then nondimensionlize the non-zero forcing term in 16 so that all variables are guaranteed to be dimensionless.

The initial conditions for velocity, vorticity and streamfunctions are trivially set as $\mathbf{U} = 0, \Omega = 0$, and $\Psi = 0$ at $t = 0$ as there's initially no flow or stream inside the cell. Rigorously speaking, the initial streamfunction term Ψ can be any constant value C (and assumed zero in our model, without loss of generality) as only its gradient is involved in the equations, which is set as zero because initial velocity should be zero. We'll later see that the same logic applies for the boundary values of Ψ.

Our model starts with a heat source heating the bottom of the cell, a "cooling source" absorbing heat at the top of the cell, and all the other parts of the cell remaining uninfluenced. However we tilt and rotate the cell, the heating/cooling sources are assumed to be fixed to the bottom/top of the cell. To mathematically express this initial temperature field, we write $\theta(x,y) = (1-y) + 10^{-6}e^{-10((x-0.5)^2+(y-0.95)^2)}$ so that the initial temperature at the bottom $y = 0$ is around 1 and decreases (almost linearly) along the y-axis until reaching the coldest value 0 at the top $y = 1$ of the cell. With the perturbation in temperature, fluids will start flowing owing to different density/gravity amplitudes.

As we assume the external heat source continues to exert its influence upon the bottom of the cell and the top of the cell is maintained cooled, we may set the Dirichlet conditions for the dimensionless tempera-

tures θ at the top ($y = 1$) and bottom ($y = 0$) of the cell to be respectively 0 and 1. For the left and right sides, we set the Neumann conditions $\theta_{\mathbf{n}} = \theta_x = 0$ because the sides are considered insulated and provide no heat source, and the actual temperature values are unpredictable.

As for the streamfunction, we have both the Neumann condition: $\Psi_{\mathbf{n}} = 0$ and Dirichlet condition: $\Psi = 0$ that holds on $\partial D = \{(x, y)|x \in \{0, 1\} \text{ or } y \in \{0, 1\}\}$, which comes from the direct fact that no flow is passing on the sides with a direction either parallel or perpendicular to these sides. We can check that the Dirichlet and Neumann conditiosn for Ψ are valid. That is, the Dirichlet conditions are continuous on the four corners; the Neumann conditions are compatible with the rates of change (derivatives) of Dirichlet conditions along directions parallel, instead of perpendicular, to each side; and the similarly derived derivatives for the Neumann conditions themselves are also continuous on the four corners.

Finally, it comes that there's no confirmed boundary conditions for vorticity Ω because it results from the curl product of velocity $\mathbf{U}$ on ∂D, meaning that the partial derivative of $\mathbf{U}$ should be computed which requires information of changeable velocity in the inner domain $D\backslash\partial D$. This differs from the secured initial condition of Ω which derives from complete information of $\mathbf{U}$ over the entire domain D at time $t = 0$. Nevertheless, with the compatibility of boundary conditions, we're able to conduct the Chebyshev-Chebyshev method in section 3 to transform the Neumann conditions for streamfunction into Dirichlet conditions for vorticity and then solve the equations for the both variables.

Finally, introducing the Prandtl number $\text{Pr} = \frac{\nu}{\kappa_T}$ and Rayleigh number $\text{Ra} = \frac{g\alpha_T(T_1-T_2)H^3}{\kappa_T\nu}$ (H denotes the height of the cell), we also obtain the dimensionless form of the forcing term in the vorticity equation 16 $\cos\alpha\text{PrRa}\theta_x - \sin\alpha\text{PrRa}\theta_y$. This wraps up our nondimensionalization of all equations to be solved.

Remark 1. *The nondimensionalized system of partial differential equations for the velocity vector, temperature, vorticity, and streamfunction goes as:*

$$\theta_t + \boldsymbol{U}\cdot\nabla\theta - \Delta\theta = 0, \tag{24}$$

$$\Omega_t + \boldsymbol{U}\cdot\nabla\Omega - Pr\Delta\Omega = \cos\alpha PrRa\theta_x - \sin\alpha PrRa\theta_y, \tag{25}$$

$$\Delta\Psi + \Omega = 0, \tag{26}$$

$$\theta = 1 \ at\ y = 1; \theta = 0 \ at\ y = 0; \theta_{\boldsymbol{n}} = 0 \ at\ x \in \{0, 1\}, \tag{27}$$

$$\Psi = \Psi_{\boldsymbol{n}} = 0 \ on\ \partial D, \tag{28}$$

$$\begin{cases} \Psi = \Omega = 0 \ at \ t = 0, \\ \theta(x,y) = (1-y) + 10^{-6} e^{-10((x-0.5)^2+(y-0.95)^2)}. \end{cases} \tag{29}$$

.

In the rest of the paper, we'll discretize and solve this system of equations to extract statistics of fluid velocity and heat transfer in our Rayleigh-Bénard convection system. In the sections after 3.1, all methods we're using can be looked up in [20].

3 Methods

Instead of approaching the set of PDEs analytically, we aim to compute approximated solutions to the equations by applying them to existing discretization schemes, with which we then reduce all equations to the form of numerically solvable Helmholtz equations.

3.1 Discretization Scheme

As we numerically approach the PDEs, we decompose the continuous dimension of time into discrete timesteps, and then we deduce solutions for the equations in the form of function values (temperature, velocity, vorticity, streamfunction) computed for a set of discrete points on the xy-plane. The equation is converted into a recurrence relation, where secured solutions for discrete points in former timesteps contribute to solutions in later timesteps. The error of the approximated solution to the actual continuous one will diminish as the size of the timestep tends to zero, but only when the discretization points and the recurrence relations are exquisitely chosen.In our model, we apply the equations 24 and 25 to the semi-implicit Adams-Bashforth/Backward-Differentiation (AB/BDI2) scheme.

Theorem 7 (AB/BDI2 Scheme)**.** *For the temeprature equation 24, fixing a size of the timestep Δt, the discretized version of the equation is written as*

$$\frac{3\theta^{n+1} - 4\theta^n + \theta^{n-1}}{2\Delta t} + 2(\boldsymbol{U}^n \cdot \nabla\theta^n) - (\boldsymbol{U}^{n-1} \cdot \nabla\theta^{n-1}) = \Delta\theta^{n+1}, \tag{30}$$

where $q^{n+k}(x,y), k \in \mathbb{Z}$ describes the function value $q(x,y)$ at the $(n+k)$th timestep.

Proof. Detailed explanations for the AB/BDI2 scheme can be found in [23]. □

Now, by moving the terms of θ^{n+1} to the left hand side of the equation and the rest of the terms to the right, we'll obtain the Helmholtz equation:

$$\Delta\theta^{n+1} - \frac{3}{2\Delta t}\theta^{n+1} = 2(\mathbf{U}^n \cdot \nabla\theta^n) - (\mathbf{U}^{n-1} \cdot \nabla\theta^{n-1}) - \frac{2\theta^n}{\Delta t} + \frac{1}{2\Delta t}\theta^{n-1}. \tag{31}$$

Similarly, the vorticity equations 16 becomes

$$\Delta\Omega^{n+1} - \frac{3}{2\mathrm{Pr}\Delta t} = \frac{1}{\mathrm{Pr}}(2(\mathbf{U}^n \cdot \nabla\Omega^n) - (\mathbf{U}^{n-1} \cdot \nabla\Omega^{n-1}) - \frac{2\Omega^n}{\Delta t} + \frac{\Omega^{n-1}}{2\Delta t} - (\cos\alpha \mathrm{PrRa}\theta_x^{n+1} - \sin\alpha\,\mathrm{Pr\,Ra}\theta_y^{n+1})). \tag{32}$$

It's notable that the equation 21 already takes the form of a Helmholtz equation, so the discretization of the streamfunction equation and its boundary conditions are written as

$$\Delta\Psi^n = -\Omega^n, \tag{33}$$

$$\begin{cases} \forall y \in 0, 1, \Psi^n(x, y) = 0, \\ \forall (x, y) \in \partial D, \Psi^n_{\mathbf{n}}(x, y) = 0. \end{cases} \tag{34}$$

Correspondingly, the initial conditions are written as

$$\begin{cases} \theta^{-1}(x, y) = \theta^0(x, y) = (1 - y) + 10^{-6} e^{-10((x-0.5)^2 + (y-0.95)^2)}, \\ \Omega^{-1} = \Omega^0 = \mathbf{U}^{-1} = \mathbf{U}^0 = \Psi^0 = 0, \end{cases} \tag{35}$$

and the boundary conditions become

$$\begin{cases} \forall y = 1, n \in \mathbb{N}, \theta^n(x, y) = 1; \forall y = 0, n \in \mathbb{N}, \theta^n(x, y) = 0, \\ \forall x \in \{0, 1\}, n \in \mathbb{N}, \theta^n_{\mathbf{n}}(x, y) = 0, \end{cases} \tag{36}$$

where $n \in \mathbb{N}$.

At timestep $n + 1$, all terms in 31 and 32 with index n and $n - 1$ are known, so the equations take the form of a Helmholtz equation ($\Delta q - \sigma q = r$ for some coefficient σ and function term r). To start an AB/BDI2 scheme, we require both q^0 and q^{-1}, therefore we equate the values of both terms to the pre-assumed initial conditions, as is shown in 35. Logically, knowing the initial data $\mathbf{U}^{-1}$,$\mathbf{U}^0$, θ^{-1}, and θ^0 triggers the subsequent recursive steps in obtaining values θ^{n+1},$\mathbf{U}^{n+1}$,Ω^{n+1}, and Ψ^{n+1} for all integer n.

Remark 2. *The procedure of solving all unknown variables in the Navier-Stokes-Boussinesq equations goes as follows. We deduce, combining* $\boldsymbol{U}^{-1}, \boldsymbol{U}^0$, θ^{-1}, *and* θ^0, *the temperature* θ^1 *by the equation 31. Then we apply* θ^1 *and the initial vorticity* Ω^0 *and* Ω^{-1} *to 32 to deduce vorticity* Ω^1. Ω^1 *is immediately applied to 33 to solve* Ψ^1 *and derive* $\boldsymbol{U}^1$ *by partial differentiation, which then contributes to solving* θ^2 *by 31. From then on, we take the recursive steps to circularly solve the values* θ^{n+1}, Ω^{n+1}, Ψ^{n+1}, *and* $\boldsymbol{U}^{n+1}$ *(*$n \in \mathbb{N}$*) with the boundary conditions at hand.*

The equation we're solving is always a Helmholtz equation, except for solving Ω which lacks a boundary condition. In that case, the Chebyshev-Chebyshev method described in 3.3 is first applied to generate the boundary condition we need so we can then adopt the general method in 3.2 to solve Helmholtz equations.

3.2 Helmholtz Equation

As mentioned, the Helmholtz Equation takes the general form

$$\forall (x, y) \in D, \Delta u(x, y) - \sigma u(x, y) = f(x, y), \tag{37}$$

with arbitrary coefficient σ, function term f, and Robin boundary data (including Dirichlet and Neumann boundary conditions as special scenarios)

$$\forall (x, y) \in \partial D, \alpha u(x, y) + \beta u_{\mathbf{n}}(x, y) = g(x, y), \tag{38}$$

for function term g and arbitrary coefficients α and β which are fixed on one side of the boundary, but may differ when switched to another side.

To numerically solve the Helmholtz equation with Robin boundary conditions, we basically adopt the Chebyshev collocation methods. Taking the Gauss-Lobatto points

$$G_{N_x, N_y} = \{(x_i, y_j) | x_i = \frac{\cos \frac{\pi i}{N_x} + 1}{2}, y_j = \frac{\cos \frac{\pi j}{N_y} + 1}{2}, i = 0, \ldots, N_x, j = 0, \ldots, N_y\}, \tag{39}$$

where N_x and N_y are arbitrarily chosen numbers reflecting the scale of fineness of our approximation (by default we set both values as 256), and denoting $u_{N_x, N_y}(x_i, y_j) = u(x_i, y_j)$ for the discrete collocation points,

we aim to solve the collocation equations

$$\begin{cases} \partial_{xx}(u_{N_x,N_y})(x_i,y_j) + \partial_{yy}(u_{N_x,N_y})(x_i,y_j) + \sigma u_{N_x,N_y}(x_i,y_j) = f(x_i,y_j), i \in \{1,\dots,N_x-1\}, j \in \{1,\dots,N_y-1\}, \\ \alpha_{up} u_{N_x,N_y}(x_i,y_{N_y}) + \beta_{up}\partial_y(u_{N_x,N_y})(x_i,y_{N_y}) = g_{up}, i \in \{1,\dots,N_x-1\}, \\ \alpha_{down} u_{N_x,N_y}(x_i,y_0) + \beta_{up}\partial_y(u_{N_x,N_y})(x_i,y_0) = g_{down}, i \in \{1,\dots,N_x-1\}, \\ \alpha_{left} u_{N_x,N_y}(x_0,y_j) + \beta_{left}\partial_x(u_{N_x,N_y})(x_0,y_j) = g_{left}, j \in \{1,\dots,N_y-1\}, \\ \alpha_{right} u_{N_x,N_y}(x_{N_x},y_j) + \beta_{right}\partial_x(u_{N_x,N_y})(x_{N_x},y_j) = g_{right}, j \in \{1,\dots,N_y-1\}, \end{cases} \tag{40}$$

where function values for inner collocation points satisfy 37 and inner boundary collocation points (collocation points on the boundary except the four corners) satisfy the boundary conditions 38.

We can solve the collocation equations 40 by expanding the partial derivative terms so that we can later convert the system of equations into one matrix equation.

Theorem 8. *With the Gauss-Lobatto points 39 chosen, the first and second order partial differentiation terms in 40 can be approximated as:*

$$\begin{cases} \partial_x(u_{N_x,N_y})(x_i,y_j) = \sum_{r=0}^{N_x} d^{(1)}_{x,i,r} u_{N_x,N_y}(x_r,y_j), \\ \partial_{xx}(u_{N_x,N_y})(x_i,y_j) = \sum_{r=0}^{N_x} d^{(2)}_{x,i,r} u_{N_x,N_y}(x_r,y_j), \\ \partial_y(u_{N_x,N_y})(x_i,y_j) = \sum_{r=0}^{N_y} d^{(1)}_{y,j,r} u_{N_x,N_y}(x_i,y_r), \\ \partial_{yy}(u_{N_x,N_y})(x_i,y_j) = \sum_{r=0}^{N_y} d^{(2)}_{y,j,r} u_{N_x,N_y}(x_i,y_r), \end{cases} \tag{41}$$

with an error bounded by $O(\frac{1}{N^2})$, where $N = \min(N_x, N_y)$.
Specifically, expressions for d terms vary among orders of differentiation and indices like x,i,r or y,j,r. To avoid repetition, we present example expressions in this theorem:

$$\begin{cases} d^{(1)}_{x,i,r} = 2\frac{c_i}{c_r}\frac{(-1)^{i+r}}{x_i - x_r} \text{ for } i,r = 0,\dots,N_x \text{ and } i \neq r, \text{ where } c_0 = c_{N_x} = 2 \text{ and } c_r = 1 \text{ for } r \in \{1,\dots,N_x-1\}, \\ d^{(2)}_{y,j,j} = -2\frac{(N_y^2-1)(1-y_j^2)+3}{3(1-y_j^2)^2} \text{ for } j \in \{1,\dots,N_y-1\}. \end{cases} \tag{42}$$

Proof. The expansion terms essentially derive from the forms

$$u_{N_x,N_y}(x,y_j) = \sum_{i=0}^{N_x} h_{x,i}(x) u(x_i,y_j), \tag{43}$$

$$u_{N_x,N_y}(x_i,y) = \sum_{j=0}^{N_y} h_{y,j}(y)u(x_i,y_j), \tag{44}$$

where $u_{N_x,N_y}(x,y)$ are constructed as Lagrange Interpolation Polynomials [23] that pass through the collocation points (x_i,y_j) in G_{N_x,N_y}. Taking first and second order partial differentiation to 43 and 44 renders the values of the d terms which only depend on the values of N_x and N_y and the coordinates of the collocation points. More details are presented in [20]. □

Notice that 41 is also adopted when we take the gradient of θ^n,θ^{n-1} (Ω^n,Ω^{n-1}) to formulate the equation for θ^{n+1} (Ω^{n+1}) or the partial derivative of Ψ^n and Ψ^{n-1} when we're computing the velocities $\mathbf{U}^n$ and $\mathbf{U}^{n-1}$. In other words, the expansion 41 generally describes the derivatives of a function on discrete collocation points, where we replace u with the term we're solving.

Applying the d terms to the expansions 41 and then applying the expansion terms to 40, we eventually obtain an algebraic system for the unknowns $\mathcal{U} = \{u_{N_x,N_y}(x_i,y_j)|i \in \{1,\dots,N_x-1\}, j \in \{1,\dots,N_y-1\}\}$, and we can solve these unknowns in a matrix equation.

Theorem 9. *We can convert 40 within approximation 41 into the matrix equation:*

$$\mathcal{A}_x\mathcal{U} + \mathcal{U}\mathcal{A}_y^T - \sigma\mathcal{U} = \mathcal{H}. \tag{45}$$

where $\mathcal{A}_x$, $\mathcal{A}_y$, and $\mathcal{H}$ are all pieced together by the d,α,β terms as well as boundary condition terms g. A typical example is $H = \begin{pmatrix} h_1 & h_2 & \dots & h_{N_y-1} \end{pmatrix}$ is a $N_x-1 \times N_y-1$ matrix, where $h_j = [h_{i,j}], i \in \{1,\dots,N_x-1\}, j \in \{1,\dots,N_y-1\}$ is an (N_x-1)-dimensional vector with

$$\begin{aligned} h_{i,j} = f(x_i,y_j) - [(\alpha_{left} + \beta_{left}d^{(1)}_{x,N_x,N_x})(\alpha_{right} + \beta_{right}d^{(1)}_{x,0,0}) - (\beta_{right}d^{(1)}_{x,0,N_x})(\beta_{left}d^{(1)}_{x,N_x,0})]^{-1} * \\ \{[(-\beta_{right}d^{(1)}_{x,0,N_x}g_{left} + (\alpha_{left} + \beta_{left}d^{(1)}_{x,N_x,N_x})g_{right})d^{(2)}_{x,i,0}] \\ +[(\alpha_{right} + \beta_{right}d^{(1)}_{x,0,0})g_{left} - \beta_{left}d^{(1)}_{x,N_x,0}g_{right}d^{(2)}_{x,i,N_x}]\} \\ -[(\alpha_{up} + \beta_{up}d^{(1)}_{y,N_y,N_y})(\alpha_{down} + \beta_{down}d^{(1)}_{y,0,0}) - (\beta_{down}d^{(1)}_{y,0,N_y})(\beta_{up}d^{(1)}_{y,N_y,0})]^{-1} * \\ \{[(-\beta_{down}d^{(1)}_{y,0,N_y}g_{up} + (\alpha_{up} + \beta_{up}d^{(1)}_{y,N_y,N_y})g_{down})d^{(2)}_{y,j,0}] \\ +[(\alpha_{down} + \beta_{down}d^{(1)}_{y,0,0})g_{up} - \beta_{up}d^{(1)}_{y,N_y,0}g_{down}d^{(2)}_{y,j,N_y}]\}. \end{aligned} \tag{46}$$

With the help of theorem 9, the rest of the steps in solving the Helmholtz equation are direct linear algebra tricks. By diagonalization, the matrices $\mathcal{A}_x$ and $\mathcal{A}_y$ are decomposed into $\mathcal{A}_x = \mathcal{P}\mathcal{D}_x\mathcal{P}^{-1}$, $\mathcal{A}_y = \mathcal{Q}\mathcal{D}_y\mathcal{Q}^{-1}$ where the columns of $\mathcal{P}$ and $\mathcal{Q}$ include the eigenvectors for $\mathcal{A}_x$ and $\mathcal{A}_y$ while the diagonals of $\mathcal{D}_x$

and $\mathcal{D}_y$ consist of the corresponding eigenvalues.

To cancel out the terms $\mathcal{A}_x$ and $\mathcal{A}_y$ from the equation 45, we introduce $\hat{\mathcal{U}} = \mathcal{P}^{-1}\mathcal{U}(\mathcal{Q}^T)^{-1}$ and left multiply 45 with $\mathcal{P}^{-1}$ and right multiply 45 with $(\mathcal{Q}^\mathcal{T})^{-1}$, therefore obtaining

$$\mathcal{D}_x\hat{\mathcal{U}} + \hat{\mathcal{U}}\mathcal{D}_y - \sigma\mathcal{U} = \mathcal{P}^{-1}\mathcal{H}(\mathcal{Q}^\mathcal{T})^{-1}. \tag{47}$$

The revised version of the matrix equation 47, with the matrix $\hat{\mathcal{U}}$ multiplied with either a diagonal matrix or a scalar constant, indicates a direct solution to every element $\hat{u_{i,j}}, i \in \{1, \ldots, N_x - 1\}, j \in \{1, \ldots, N_y - 1\}$ of $\hat{\mathcal{U}}$ by division:

$$\hat{u}_{i,j} = \frac{\hat{h_{i,j}}}{\lambda_{x,i} + \lambda_{y,j} - \sigma}, \tag{48}$$

where $\hat{h}_{i,j}$ denotes every element of $\hat{\mathcal{H}} = \mathcal{P}^{-1}\mathcal{H}(\mathcal{Q}^\mathcal{T})^{-1}$, while $\lambda_{x,i}$ and $\lambda_{y,j}$ denote the ith/jth eigenvalue recorded in the diagonal matrices $\mathcal{D}_x$ and $\mathcal{D}_y$.

After we derive $\hat{\mathcal{U}}$, we can compute $\mathcal{U} = \mathcal{P}\hat{\mathcal{U}}$ for the inner collocation points. These function values can be combined with the d, α, β, and g terms mentioned above and applied to the boundary conditions in 40 to finally derive the boundary values $u_{N_x,N_y}(x_i, y_j), (x_i, y_j) \in \partial D$. This completes our objective, given the Helmholtz equation 37 and boundary conditions 38, to solve the function values at all collocation points $(x_i, y_j) \in G_{N_x,N_y}$ which approximate an actual solution.

3.3 Chebyshev-Chebyshev Method

We adopt the general procedure to solve the Helmholtz equations within the AB/BDI2 schemes. However, an exception arises when we're solving the Helmholtz equations32 and 33, as there's no usable boundary condition for vorticity Ω^{n+1} but we have both a Dirichlet and a Neumann boundary condition for stream-function Ψ^{n+1}. In this case, we utilize the Chebyshev-Chebyshev method explained in [20] to solve both Helmholtz equations altogether.

Simplifying the equations, we obtain a system in the general form

$$\begin{cases} \Delta\Omega - \sigma\Omega = f \text{ in } D, \\ \Delta\Psi = -\Omega \text{ in } D, \\ \Psi = g \text{ on } \partial D, \\ \Psi_{\mathbf{n}} = h \text{ on } \partial D. \end{cases} \tag{49}$$

which we've secured the compatibility of boundary conditions of Ψ. The system of equations is hard to approach directly, but we can break down the system into two parts and solve each separately, and finally add up the solutions from each part of PDEs to obtain the solution we want.

Theorem 10. *The system can be decomposed into the $\tilde{\mathcal{P}}$ problem:*

$$\begin{cases} \Delta\tilde{\Omega}_{N_x,N_y} - \sigma\tilde{\Omega}_{N_x,N_y} = f, \\ \Delta\tilde{\Psi}_{N_x,N_y} = -\tilde{\Omega}_{N_x,N_y}, \\ \tilde{\Omega}_{N_x,N_y} = 0 \ \textit{at } \partial D, \\ \tilde{\Psi}_{N_x,N_y} = g \ \textit{at } \partial D, \end{cases} \tag{50}$$

and the $\bar{\mathcal{P}}$ problem:

$$\begin{cases} \Delta\bar{\Omega}_{N_x,N_y} - \sigma\bar{\Omega}_{N_x,N_y} = 0, \\ \Delta\bar{\Psi}_{N_x,N_y} = -\bar{\Omega}_{N_x,N_y}, \\ \bar{\Psi}_{N_x,N_y} = 0 \ \textit{at } \partial D, \\ \partial\boldsymbol{n}\bar{\Psi}_{N_x,N_y} = h - \partial\boldsymbol{n}\tilde{\Psi}_{N_x,N_y} \ \textit{at } \partial D. \end{cases} \tag{51}$$

Summing up solutions to both problems render the solution to the system:

$$\begin{cases} \Omega_{N_x,N_y} = \tilde{\Omega}_{N_x,N_y} + \bar{\Omega}_{N_x,N_y}, \\ \Psi_{N_x,N_y} = \tilde{\Psi}_{N_x,N_y} + \bar{\Psi}_{N_x,N_y}. \end{cases} \tag{52}$$

In theorem 10, the $\tilde{\mathcal{P}}$ problem is directly solvable – we only have to solve the Helmholtz equations for the Ω terms and then apply it to the Helmholtz equations for the Ψ terms. Boundary data for both terms are sufficiently provided. The main difficulty arises when we're solving the Ω term in the $\bar{\mathcal{P}}$ problem where

there's no given boudary data, and we try to transform the Neumann condition for $\bar{\Psi}_{N_x,N_y}$ into an equivalent Dirichlet condition: $\bar{\Omega}_{N_x,N_y} = \xi$.

Assuming such a condition already holds, then we can adopt the general operations of linear superposition and expand the function $\bar{\Omega}_{N_x,N_y}$ as a weighted summation of component functions $\bar{\Omega}_l$, where each component function takes value 0 over all but one boundary collocation point, and takes value 1 over the one designated point.

Writing as mathematical expressions, there's that $\bar{\Omega}_{N_x,N_y} = \sum_{l=1}^{L} \xi_l \bar{\Omega}_l$ and $\bar{\Psi}_{N_x,N_y} = \sum_{l=1}^{L} \xi_l \bar{\Psi}_l$, and $\bar{\Omega}_l$, $\bar{\Psi}_l$ satisfy:

$$\begin{cases} \Delta\bar{\Omega}_l - \sigma\bar{\Omega}_l = 0 \text{ in } D, \\ \bar{\Omega}_l|_{\eta_m} = \delta_{m,l} \text{ for collocation point } \eta_m \text{ on } \partial D, m \in 1, \ldots, 2(N_x + N_y - 2), \\ \Delta\bar{\Psi}_l = -\bar{\Omega}_l \text{ in } D, \\ \bar{\Psi}_l|_{\eta_m} = 0 \text{ for } \eta_m \in \partial D, \end{cases} \tag{53}$$

which we name as the $\bar{\mathcal{P}}_l$-problem.

Notice that L is an arbitrarily taken scale value like N_x and N_y which reflects the fineness of the numerical solution. Applying the solutions $\bar{\Psi}_l$ back to the $\bar{\mathcal{P}}$-problem, we obtain the equation

$$\sum_{l=0}^{L} (\partial_{\mathbf{n}} \bar{\Psi}_l|_{\eta_m}) \xi_l = (h - \partial_{\mathbf{n}} \tilde{\bar{\Psi}}_{N_x,N_y})|_{\eta_m}, m \in \{1, \ldots, L\}, \tag{54}$$

which again can be re-written as a matrix equation

$$\mathcal{M}\Xi = \tilde{H}. \tag{55}$$

As $l = 1, 2, \ldots, L$, there're in all L $\bar{\mathcal{P}}_l$ problems to solve. But just like the $\tilde{\mathcal{P}}$ problem 50, every $\bar{\mathcal{P}}_l$ problem 53 is also directly solvable by methods in 3.2. With the solutions from both problems, we can finally obtain the influence matrix $\mathcal{M}$:

$$\mathcal{M} = \begin{pmatrix} \partial_{\mathbf{n}} \bar{\Psi}_0|_{\eta_1} & \partial_{\mathbf{n}} \bar{\Psi}_1|_{\eta_1} & \ldots & \partial_{\mathbf{n}} \bar{\Psi}_L|_{\eta_1} \\ \partial_{\mathbf{n}} \bar{\Psi}_0|_{\eta_2} & \partial_{\mathbf{n}} \bar{\Psi}_1|_{\eta_2} & \ldots & \partial_{\mathbf{n}} \bar{\Psi}_L|_{\eta_2} \\ \ldots & \ldots & \ldots & \ldots \\ \partial_{\mathbf{n}} \bar{\Psi}_0|_{\eta_L} & \partial_{\mathbf{n}} \bar{\Psi}_1|_{\eta_L} & \ldots & \partial_{\mathbf{n}} \bar{\Psi}_L|_{\eta_L} \end{pmatrix}, \tag{56}$$

and the $\tilde{H}$ term:

$$\tilde{H} = \begin{pmatrix} (h - \partial_{\mathbf{n}}\tilde{\Psi}_{N_x,N_y})|_{\eta_1} & (h - \partial_{\mathbf{n}}\tilde{\Psi}_{N_x,N_y})|_{\eta_2} & \dots & (h - \partial_{\mathbf{n}}\tilde{\Psi}_{N_x,N_y})|_{\eta_L} \end{pmatrix}^T, \tag{57}$$

and solve $\Xi = \begin{pmatrix} \xi_1 & \xi_2 & \dots & \xi_L \end{pmatrix}^T = \mathcal{M}^{-1}\tilde{H}$. Note that to compute the partial derivative terms $\partial_{\mathbf{n}}\bar{\Psi}_a|\eta_b$, we only need to apply the expressions in theorem 8 to approximate $\partial_{\mathbf{n}}\bar{\Psi}_a$ over the collocation point η_b.

With the ξ values at hand, we can solve the Helmholtz equation 50 where the boundary condition related with the Ψ term is now replaced by $\bar{\Omega}_{N_x,N_y}(\eta_m) = \xi_m$ at ∂D $(1 \leqslant m \leqslant L)$. Eventually, the solutions for vorticity and streamfunction at all collocation points are obtained by the summation $\Omega_{N_x,N_y} = \tilde{\Omega}_{N_x,N_y} + \bar{\Omega}_{N_x,N_y}$. This completes our solving of the equation form 49.

Remark 3. *Notice that to make the bar problem 51 solvable with sufficient boundary data $\xi_m (1 \leqslant m \leqslant L)$ for Ω, we initially set $L = 2(N_x + N_y - 2)$ the number of inner boundary collocation points. However, the matrix $\mathcal{M}$ obtained in this way is not invertible, and [20] provides the resolution of further removing four designated collocation points from our computation to make all eigenvalues in the influence matrix non-zero, therefore making $L = 2(N_x + N_y - 4)$.*

4 Results

We implement the entire procedure from section 2 to section 3 in Matlab. In the experiment, we set the Rayleigh number Ra $= 10^8$ and Prandtl number Pr $= 4.4$, and we model the convection cell under counterclockwise rotation ranging from 0° to 180° with 5° as the step size ($\alpha \in \{5k | k \in \mathbb{N}, 0 \leqslant k \leqslant 36\}$).

Within discretization, we set $N_x = N_y = 256$ which indicates 256^2 collocation points over the convection cell, and we set maximum timestep $t_{max} = 10^6 - 1$. This implies that for each tilt angle α, we model the flowing of fluids, starting from its initial condition $t = 0$, up to $t = 10^6 - 1$ discrete units of time. In accordance with the time size, the Matlab program iteratively solves $10^6 - 1$ sets of discretized equations 30 - 36, and always plug the former recorded solution/initial values for temperatures θ^{n-1},θ^n, velocities $\mathbf{U}^{n-1}$, $\mathbf{U}^n$, and vorticity values Ω^{n-1}, Ω^n into the current equations at the $(n+1)$th timestep.

We directly adopt the method in section 3.2 to solve the equation for temperature θ, setting f in equation 37 to be the right-hand-side term in equation 31 and $\alpha = 0, \beta = 1, g = 0$ for the left and right

side boundaries and $\alpha = 1, \beta = 0, g = 0$ for the top and bottom boundaries in equation 38, as a reference to 36. Similarly, as we solve the Helmholtz equations for vorticity and streamfunction 49 with the help of the Chebyshev-Chebyshev method, we set the f term according to equation 32 and boundary conditions $g = h = 0$ referring to 34.

Apart from the recorded values for the temperature, velocity, vorticity, and streamfunction unknowns, we also record the Reynolds number Re, Nusselt number Nu, and system net angular momentum L at the end of every iteration.

Definition 3 (Reynolds Number)**.**

$$Re^{n+1} = \frac{\max(\{(U^{n+1}(x_i, y_j)^2 + V^{n+1}(x_i, y_j)^2) | (x_i, y_j) \in G_{N_x, N_y}\})}{Pr}. \tag{58}$$

The Reynolds number Re measures the maximum possible amplitude of fluid flow speed inside the cell at timestep $t = n + 1$, as a reflection of how turbulent the viscous fluids can potentially become through time after being heated and tilted.

Definition 4 (Nusselt Number)**.**

$$Nu = \int_0^1 \theta_{\boldsymbol{n}}(x, 1, t)dx. \tag{59}$$

The Nusselt number describes the total heat flux passing across the cell on the y-axis at $y = 1$ and reflects how heat originating from the bottom heat source propagates and maintains its influence to flowing fluids at the coldest top.

In the discrete sense, we compute integration also with the help of d terms in section 3.2. As $\mathcal{A}_x$ is an $N_x - 1 \times N_x - 1$ matrix where $[\mathcal{A}_x]_{i,j} = d_{x,i,j} (1 \leqslant i, j \leqslant N_x - 1)$, we take the inverse of $\mathcal{A}_x$ and denote $d^{-1}_{x,i,j} = [\mathcal{A}_x^{-1}]_{i,j}$, so that

$$\mathrm{Nu}^{n+1} = \sum_{j=1}^{N_x - 1} d^{-1}_{x,1,j} \theta_y^{n+1}(x_j, y_0) = \sum_{j=1}^{N_x - 1} d^{-1}_{x,1,j} \sum_{r=0}^{N_y} d^{(1)}_{y,0,r} \theta^{n+1}(x_j, y_r), \tag{60}$$

takes the value from θ^{n+1} and the d terms.

Definition 5 (System Total Angular Momentum)**.**

$$L(t) = \int_0^1 \int_0^1 ((x - 0.5)V(x, y, t) - (y - 0.5)U(x, y, t))dxdy. \tag{61}$$

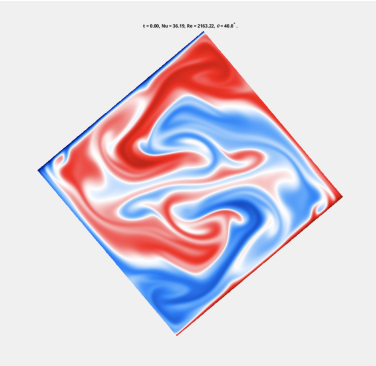

Figure 2: GIF animation of Tilted Convection Cell

Finally, we calculate total angular momentum in the system which, in the discrete version, is written as

$$L^{n+1} = \sum_{i=1}^{N_x-1} \sum_{j=1}^{N_y-1} ((x_i - 0.5)V^{n+1}(x_i, y_j) - (u_j - 0.5)U^{n+1}(x_i, y_j)). \tag{62}$$

We've chosen $(0.5, 0.5)$ as the "origin" point where the fluid particle with unit mass flows around and holds a dimensionless angular momentum. The value of the angular momentum is therefore exactly the cross product of position relative to the origin and the 2-dimensional velocity $\mathbf{U}$. Overall, the three output values Re, Nu, and L represent the features of fluid flows inside the convection cell which change along with the tilting angle from 0° to 180°. For each of the 10^6 timesteps, one output value is recorded so we eventually obtain the outputs in the form of 10^6-dimensional vectors.

We use Python codes to extract and process the recorded outputs, in which we take the average of values after the $10^6/2$th timestep. The average is taken because we assume the system with a perturbed initial temperature field has gradually stabilized throughout the former half of the entire convection process and converged to a state in the latter half where the turbulent flows are either becoming static or circulating around the cell in cycles. Specifically for total angular momentum, we take the root mean square average because the L values oscillate around zero and take positive and negative values which cancel out each other in the computation of the arithmetic mean. It should also be notified that we don't need to have similar concerns with the Re or Nu values because they're defined to be always positive. If we alternatively define L as the absolute value of the integral, we can also directly apply the arithmetic mean. In all, there's a high level of freedom in dealing with the statistics.

Apart from output values, we also use Matlab to output GIF animations 2 which present the dynamic variation of the temperature field of the square convection cell, given every possible tilting angle. The bottom

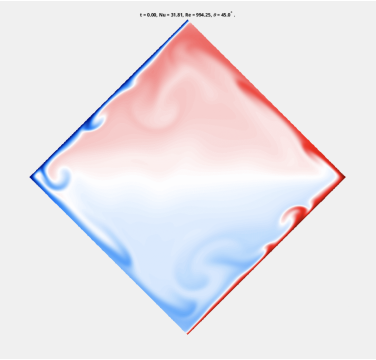

Figure 3: Tilted 45° Counter-Clockwise

of the cell influenced by the heat source is dyed dark red and the cooling part at the top is dyed blue. As time passes, it's viewable from the animations that red parts of the fluid advance upwards into the bluish area because of lower densities (and buoyant impacts) compared with blue parts, and the fluids with high and low temperatures intermix together and create white regions inferring a moderate temperature $\theta = 0.5$.

As will be discussed in the following parts, for a certain range of tilting angles, the active joining and rotating of red and blue areas will gradually come to a rest as the entire temperature field stabilize. This implies the temperature function θ is reaching a steady state where the heat entering a region carried by blobs is balanced with heat diffusion from the region to neighboring regions. As the heating/cooling sources are fixed to the bottom/top of the cell, they're always dyed dark red and dark blue however the entire cell is tilted, as are presented as thin dark red/blue stripes statically clinging to the bottom/top of the cell. Nevertheless, different tilting angles decide different patterns of flows and heat propagation in the cell which we'll observe in the following visualization section 4.1, combined with plotted results of the Re, Nu, and L outputs.

4.1 Visualized Results

Notably, as $\alpha = 45°$, the system converges into a state in figure 3 where the red and blue stripes constantly circulate along the sides of the cell, while the regions away from the margins present light red/blue colors indicating more moderate temperatures. This circulation is replaced by oscillation as exemplified in figure 4, where red parts are continuously pushed down and elevating again while the blue parts display the opposite motions. The amplitude of oscillation gradually diminishes as time passes and the system finally converges into the state where the red parts remain still at the upper half of the cell (but not the "top" of

Figure 4: Tilted 90° Counter-Clockwise (Heating/Cooling Sources on Sidewalls)

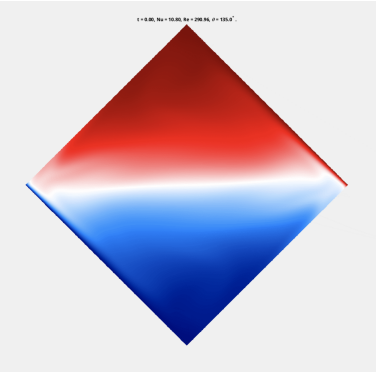

Figure 5: Tilted 135° Counter-Clockwise

the cell, which is now rotated 90° counter-clockwise) and blue parts take the rest lower half.

Similar states of convergence are also observed in figure 5 and figure 6 where the fluids turn more laminar and that it takes less and less time for the bold red and blue parts of the cell to turn steady and stay after cyclic or oscillatory activities, despite the constant influence of heating/cooling sources at the "bottom"/"top" of the cell. Specifically in figure 6, when the cell is totally upside-down, there's no moving of red or blue parts observed, and they stay at their initial locations throughout the entire time span.

For each tilt angle α, we also extract the average value of the Re, Nu, and L numbers of the stabilizing convection system and we fit the results to a plot for each number. The variation pattern of each plot as α rises from 0° to 180° provides supplementary information about fluid velocities. It's important to notice that the motion of "red/blue parts" in the previous GIF animations don't directly indicate the motion of blobs inside the cell because the blobs themselves continuously change in temperature, and we'll immediately see that there're constantly dynamic fluid activities even in steady temperature fields. In fact, the plots

Figure 6: Tilted 180° Counter-Clockwise (Upside-Down)

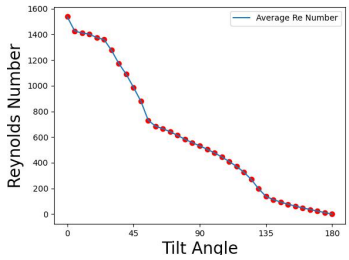

Figure 7: Reynolds - Angle Plot

reveal fluid activities unobservable from the GIF animations which provide information about the changing temperature fields, and the information combined disclose physical facts of the convection system that we can analyze and even exploit in detail in the future work.

As is displayed in figure 7 – the Re-α plot – the dimensionless Reynolds number continuously decreases from nearly 1600 to 0 while the tilt angle grows from 0° to 180°. This reveals that turbulent flows are gradually replaced by laminar ones as the cell is tilted. As we look at the corresponding GIF animation 3 when the cell is moderately tilted with $\alpha = 45°$, we can indeed find heat being carried by the speedy fluids circularly around the margins of the cell. The heated fluids accelerate and flow upward as they have thinner densities, while the cooled fluids with higher densities sediment. Both incompressible fluids hit the up and bottom of the cell and start to move in directions parallel to the left and right sides, eventually creating circulation that press close to the margins. In the case $\alpha = 45°$, this fluid activity takes a sufficiently high speed so that heat is carried along the trajectories of the moving fluids quicker than they diffuse. As a result, the temperature field in red and blue is also driven to circulate in the similar way.

The observable motion of red and blue stripes in the temperature field quickly diminishes as α grows

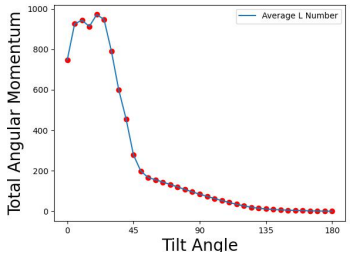

Figure 8: Net Angular Momentum - Tilt Angle Plot

to 90 degrees and higher. As observed in 4 and 5, the temperature field grows steady after momentary up-and-down oscillations of the red and blue parts. However, the Re plot 7 reveals that the fluids are still circularly rotating around the $(0.5, 0.5)$ center of the cell, implying that the delivery of heat in blobs moving around the cell is gradually balanced with the diffusion of the heat being carried. Therefore, even though the GIF animation seems static, we know from the Re plot about the dynamic fluid motions that continue within the cell.

Nonetheless, it's also observable from the plot that when α grows too high, the moving fluids also stabilize along with the dropping of the maximum possible velocity. In the extreme case when α turns 180°, there's neither fluid motion nor change of temperature field in the first place, and the whole system remains the way it's initialized.

The changing of fluid activities along the growing of α is also manifest in the figure 8 of the L plot. We can see the total angular momentum of the system which quickly plunges as the angle passes around $25 - 30$ degrees and then slowly decreasing after 45 degrees until eventually reaching 0. This directly indicates there are active circular fluid activities across the entire convection cell at low tilting angles ($\alpha < 45^\circ$), which immediately weaken but still remain moderate at degrees ranging from 45 to 135 degrees, and finally ceasing to exist at large angles ($\alpha > 135^\circ$). The statistical results of the L plot highly coincide with our observations in the Re plot and supports our narrative of the variational fluid motions aside of the changing temperature field.

Finally, another interesting observation is revealed in the Nusselt number plot in figure 9 which models how much heat is passing through the top of the cell on the y-direction (parallel to the left and right sides of the cell). It's shown that the Nusselt number continuously increases until reaching the maximum at $\alpha = 90^\circ$ (precisely when the heating and cooling sources are placed at the sidewalls instead of the top/bottom), and then swiftly drops as the angle continues to increase to 180°. It's clear that at high tilting angles, the heated fluids already at the upper part of the cell tend to remain static, so there's little heat transfer on the y

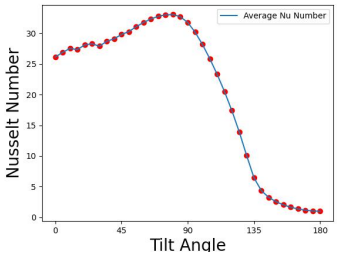

Figure 9: Nusselt Number - Tilt Angle Plot

direction.

But still, it remains a question why the largest heat flux is observed at $\alpha = 90^\circ$ where the total angular momentum L already slumps and the fluids already become laminar with a falling Reynolds number Re and rotate moderately. In fact, our finding aligns with real life applications like the radiators for computers which are always placed vertically so that heat will be most efficiently diffused from the computer equipment. To approach this finding in a scientific way, there are a series of prospective hypotheses that may explain the optimum of heat flux as we further our studies of the Rayleigh-Bénard convection model in our future work.

5 Conclusion and Overlook

In this paper, we model the dynamics of the Rayleigh-Bénard convection model – incompressible fluids in a two-dimensional tilted convection cell with fixed heating and cooling sources. We adopt the Navier-Stokes equations within Boussinesq approximation and a heat equation to model fluid turbulence and the according changes of the temperature field. We introduce the concepts of vorticity and streamfunction which provide sufficient initial and boundary data to solve the equations. The equations are mathematically discretized within the AB/BDI2 scheme and transformed into Helmholtz equations, and we introduce the Chebyshev-Chebyshev method to assist our solving of the Helmholtz equations in the discrete sense – acquiring function values at designated discrete space and time coordinates. Finally, in accordance with every tilting angle of the convection cell, we record the variation of fluid temperatures and velocities over time and present it as animations as well as plots of the Reynolds number, the Nusselt number, and the total angular momentum. It's discovered that heat flux continuously grows as the tilting angle increases, and then descends after the tilting angle reaches 90°; and circular fluid activities constantly weaken as the tilting angle constantly grows from 0° to 180°.

In the future research, we're planning to apply more Rayleigh numbers Ra and Prandtl numbers Pr and different cell sizes (so the square cell turns rectangular) to our Navier-Stokes-Boussinesq equations. In this way we can validate whether the changing patterns of Re, Nu, and L numbers of the system along different tilting angles – as we've described in last section – are maintained on distinct physical conditions of the cell. On top of these observations, we're aimed to disclose physical hypotheses that provide an explanation for questions like why an optimal amount of the Nusselt number is achieved at a tilting angle of 90 degrees and why the derivatives of the Nu, Re and L numbers (as functions of α) switches sharply around values of tilting angles like 45°, 90°, and 135°. In the end, we can prospectively extend our study of the system under a fixed tilting angle to a dynamically rotating system and study questions like maintaining a circular rotation state of the fluids or optimizing net heat flux on the y direction, as the convection cell goes on to rotate back and forth. These questions are bound to provide an insight into studies of natural processes and applications to industrial and engineering fields where thermal convection systems are intensively dealt with.

References

[1] David J Acheson. Elementary fluid dynamics, 1991.

[2] Guenter Ahlers, Siegfried Grossmann, and Detlef Lohse. Heat transfer and large scale dynamics in turbulent rayleigh-bénard convection. Reviews of modern physics, 81(2):503, 2009.

[3] Kim MJ Alards, Rudie PJ Kunnen, Herman JH Clercx, and Federico Toschi. Statistical properties of thermally expandable particles in soft rayleigh-benard convection. arXiv preprint arXiv:1907.00049, 2019.

[4] Yun Bao, Jun Chen, Bo-Fang Liu, Zhen-Su She, Jun Zhang, and Quan Zhou. Enhanced heat transport in partitioned thermal convection. Journal of Fluid Mechanics, 784:R5, 2015.

[5] Roberto Benzi and Emily SC Ching. Polymers in fluid flows. Annual Review of Condensed Matter Physics, 9:163–181, 2018.

[6] L Biferale, P Perlekar, M Sbragaglia, and FJPRL Toschi. Convection in multiphase fluid flows using lattice boltzmann methods. Physical Review Letters, 108(10):104502, 2012.

[7] Alexander Blass, Xiaojue Zhu, Roberto Verzicco, Detlef Lohse, and Richard JAM Stevens. Flow organization and heat transfer in turbulent wall sheared thermal convection. Journal of fluid mechanics, 897:A22, 2020.

[8] Jacopo Buongiorno, David C Venerus, Naveen Prabhat, Thomas McKrell, Jessica Townsend, Rebecca Christianson, Yuriy V Tolmachev, Pawel Keblinski, Lin-wen Hu, Jorge L Alvarado, et al. A benchmark study on the thermal conductivity of nanofluids. Journal of Applied Physics, 106(9):094312, 2009.

[9] Kai Leong Chong, Yantao Yang, Shi-Di Huang, Jin-Qiang Zhong, Richard JAM Stevens, Roberto Verzicco, Detlef Lohse, and Ke-Qing Xia. Confined rayleigh-bénard, rotating rayleigh-bénard, and double diffusive convection: A unifying view on turbulent transport enhancement through coherent structure manipulation. Physical review letters, 119(6):064501, 2017.

[10] Y-B Du and Penger Tong. Enhanced heat transport in turbulent convection over a rough surface. Physical review letters, 81(5):987, 1998.

[11] Mohammad S Emran and Olga Shishkina. Natural convection in cylindrical containers with isothermal ring-shaped obstacles. Journal of Fluid Mechanics, 882:A3, 2020.

[12] Shuang-Xi Guo, Sheng-Qi Zhou, Xian-Rong Cen, Ling Qu, Yuan-Zheng Lu, Liang Sun, and Xiao-Dong Shang. The effect of cell tilting on turbulent thermal convection in a rectangular cell. Journal of Fluid Mechanics, 762:273–287, 2015.

[13] Laurens E Howle. Active control of rayleigh–bénard convection. Physics of Fluids, 9(7):1861–1863, 1997.

[14] Shi-Di Huang, Matthias Kaczorowski, Rui Ni, Ke-Qing Xia, et al. Confinement-induced heat-transport enhancement in turbulent thermal convection. Physical Review Letters, 111(10):104501, 2013.

[15] Hechuan Jiang, Xiaojue Zhu, Varghese Mathai, Roberto Verzicco, Detlef Lohse, and Chao Sun. Controlling heat transport and flow structures in thermal turbulence using ratchet surfaces. Physical review letters, 120(4):044501, 2018.

[16] Tian-Cheng Jin, Jian-Zhao Wu, Yi-Zhao Zhang, Yu-Lu Liu, and Quan Zhou. Shear-induced modulation on thermal convection over rough plates. Journal of Fluid Mechanics, 936:A28, 2022.

[17] Hao-Ran Liu, Kai Leong Chong, Chong Shen Ng, Roberto Verzicco, and Detlef Lohse. Enhancing heat transport in multiphase rayleigh–bénard turbulence by changing the plate–liquid contact angles. Journal of fluid mechanics, 933:R1, 2022.

[18] Detlef Lohse and Ke-Qing Xia. Small-scale properties of turbulent rayleigh-bénard convection. Annual Review of Fluid Mechanics, 42:335–364, 2010.

[19] Jinzi Mac Huang and Jun Zhang. Rayleigh–bénard thermal convection perturbed by a horizontal heat flux. Journal of Fluid Mechanics, 954:R2, 2023.

[20] Roger Peyret. Spectral methods for incompressible viscous flow, volume 148. Springer, 2002.

[21] Antonio Piccolo, Roberto Siclari, Fabrizio Rando, and Mauro Cannistraro. Comparative performance of thermoacoustic heat exchangers with different pore geometries in oscillatory flow. implementation of experimental techniques. Applied Sciences, 7(8):784, 2017.

[22] Richard JAM Stevens, Jin-Qiang Zhong, Herman JH Clercx, Guenter Ahlers, and Detlef Lohse. Transitions between turbulent states in rotating rayleigh-bénard convection. Physical review letters, 103(2):024503, 2009.

[23] Endre Süli and David F Mayers. An introduction to numerical analysis. Cambridge university press, 2003.

[24] Srikanth Toppaladoddi, Sauro Succi, and John S Wettlaufer. Roughness as a route to the ultimate regime of thermal convection. Physical review letters, 118(7):074503, 2017.

[25] David J Tritton. Physical fluid dynamics. Springer Science & Business Media, 2012.

[26] Qi Wang, Zhen-Hua Wan, Rui Yan, and De-Jun Sun. Multiple states and heat transfer in two-dimensional tilted convection with large aspect ratios. Physical Review Fluids, 3(11):113503, 2018.

[27] Qi Wang, Zhen-Hua Wan, Rui Yan, and De-Jun Sun. Multiple states and heat transfer in two-dimensional tilted convection with large aspect ratios. Physical Review Fluids, 3(11):113503, 2018.

[28] Ziqi Wang, Varghese Mathai, and Chao Sun. Self-sustained biphasic catalytic particle turbulence. Nature communications, 10(1):3333, 2019.

[29] Jian-Zhao Wu, Yu-Hong Dong, Bo-Fu Wang, and Quan Zhou. Phase decomposition analysis on oscillatory rayleigh–bénard turbulence. Physics of Fluids, 33(4):045108, 2021.

[30] Jian-Zhao Wu, Bo-Fu Wang, Kai Leong Chong, Yu-Hong Dong, Chao Sun, and Quan Zhou. Vibration-induced 'anti-gravity'tames thermal turbulence at high rayleigh numbers. Journal of Fluid Mechanics, 951:A13, 2022.

[31] Jian-Lin Yang, Yi-Zhao Zhang, Tian-cheng Jin, Yu-Hong Dong, Bo-Fu Wang, and Quan Zhou. The-dependence of the critical roughness height in two-dimensional turbulent rayleigh–bénard convection. Journal of Fluid Mechanics, 911:A52, 2021.

[32] Rui Yang, Kai Leong Chong, Qi Wang, Roberto Verzicco, Olga Shishkina, and Detlef Lohse. Periodically modulated thermal convection. Physical review letters, 125(15):154502, 2020.

[33] Wenwu Yang, Yi-Zhao Zhang, Bo-Fu Wang, Yuhong Dong, and Quan Zhou. Dynamic coupling between carrier and dispersed phases in rayleigh–bénard convection laden with inertial isothermal particles. Journal of Fluid Mechanics, 930:A24, 2022.

[34] Shengqi Zhang, Zhenhua Xia, Quan Zhou, and Shiyi Chen. Controlling flow reversal in two-dimensional rayleigh–bénard convection. Journal of Fluid Mechanics, 891:R4, 2020.

[35] Chao-Ben Zhao, Bo-Fu Wang, Jian-Zhao Wu, Kai Leong Chong, and Quan Zhou. Suppression of flow reversals via manipulating corner rolls in plane rayleigh–bénard convection. Journal of Fluid Mechanics, 946:A44, 2022.

[36] Chao-Ben Zhao, Yi-Zhao Zhang, Bo-Fu Wang, Jian-Zhao Wu, Kai Leong Chong, and Quan Zhou. Modulation of turbulent rayleigh-bénard convection under spatially harmonic heating. Physical Review E, 105(5):055107, 2022.

[37] Jin-Qiang Zhong and Guenter Ahlers. Heat transport and the large-scale circulation in rotating turbulent rayleigh–bénard convection. Journal of fluid mechanics, 665:300–333, 2010.

[38] Xiaojue Zhu, Richard JAM Stevens, Roberto Verzicco, and Detlef Lohse. Roughness-facilitated local 1/2 scaling does not imply the onset of the ultimate regime of thermal convection. Physical review letters, 119(15):154501, 2017.